ChemComm

COMMUNICATION

View Article Online
View Journal | View Issue

Cite this: *Chem. Commun.*, 2017, 53, 4853

Received 22nd December 2016,
Accepted 11th April 2017

DOI: 10.1039/c6cc10183f

rsc.li/chemcomm

Nearest-neighbour nanocrystal bonding dictates framework stability or collapse in colloidal nanocrystal frameworks†

Teresa E. Williams,[ab] Daniela Ushizima,[c] Chenhui Zhu,[d] André Anders,[e] Delia J. Milliron [f] and Brett A. Helms *[b]

Block copolymers serve as architecture-directing agents for the assembly of colloidal nanocrystals into a variety of mesoporous solids. Here we report the fundamental order–disorder transition in such assemblies, which yield, on one hand, ordered colloidal nanocrystals frameworks or, alternatively, disordered mesoporous nanocrystal films. Our determination of the order–disorder transition is based on extensive image analysis of films after thermal processing. The number of nearest-nanocrystal neighbours emerges as a critical parameter dictating assembly outcomes, which is in turn determined by the nanocrystal volume fraction (f_{NC}). We also identify the minimum f_{NC} needed to support the structure against collapse.

Colloidal nanocrystal frameworks (CNFs) are comprised of periodic arrangements of colloidal nanocrystals (NCs) and mesoscopic pores, typically in 3-D or quasi-2-D formats.[1–9] The placement of NCs in such periodic arrangements from colloidal dispersions is initially directed by the presence of larger polymer colloids—*e.g.*, block copolymer (BCP) micelles—that typically pack into progenitor lattices with smaller NCs packing in the interstitial voids.[3,6,10–12] Simple thermal or chemical processing of solution-cast BCP–NC composites reveals the intended mesoporosity. As active layers in energy devices, CNFs have found use in electrochromic windows,[13,14] battery electrodes,[3,5] (pseudo)capacitors,[2,3,5,15–17] catalysts,[18,19] and photovoltaics.[20] In each of these applications, the manifestation of interconnected framework mesoporosity is useful in avoiding mass- or ion-transport bottlenecks throughout the film.[13,21–24]

During mesopore generation, it is desirable that the CNF retain the high degree of order present in progenitor mesostructured composite;[3,6,11,14,25,26] furthermore, the CNF should be self-supporting at the end of the procedure. It follows that the fraction of NCs (f_{NC}) in the composite could play a key role in those aspects, since chemical contacts between NC surfaces are required to buttress the framework.[3,6] A systematic approach to understanding that role quantitatively has been lacking.

Here we show that the number of nearest-neighbour contacts between NCs in the CNF is deterministic in whether the framework is self-supporting after thermal processing, or rather collapses under its own weight. Concomitant with framework collapse is loss of order, which we observe, and quantify, using top-down and cross-sectional scanning electron microscopy (SEM), and grazing incidence small-angle X-ray scattering (GISAXS). Additionally, we apply image analysis techniques to quantitatively assess an order–disorder transition, pore-size distribution within the framework, and ranges of f_{NC} yielding CNFs rather than disordered mesoporous films. The design rules laid out here indicate self-supporting films assembled from spherical NCs are feasible only when $f_{NC} > 17\%$. Furthermore, CNFs emerge only for $f_{NC} = 30–55\%$.

To understand the impact of NC nearest-neighbour contacts on framework stability during thermal processing, we attempted to prepare CNFs from BCP–NC composites loaded with variable quantities of NCs. To do so, composite thin films (240–440 nm) were cast onto Si substrates from a dispersion of cationic naked[27–29] tin-doped indium oxide NCs (d_{NC} = 5.3 ± 0.7 nm, Fig. S1, ESI†) and BCP micelles that were pre-formed in DMF : EtOH (2 : 8 v/v) from one of two polystyrene-*block*-poly(*N*,*N*-dimethylacrylamide) architecture directing agents:[3,11] PS_{60k}-*b*-$PDMA_{20k}$ (d_{BCP} = 34.4 nm ± 2.3 nm, Fig. S2, ESI†) and PS_{20k}-*b*-$PDMA_{20k}$ (d_{BCP} = 22.7 nm ± 2.3 nm, Fig. S3, ESI†). Seven loadings were prepared for each architecture-directing agent, with BCP loadings spanning 12–60% w/w (Table S1, ESI†). The composite films were thermally annealed in air (550 °C, 1.5 h) to sinter the

[a] *Graduate Group in Applied Science and Technology, University of California-Berkeley, Berkeley, CA 94720, USA*
[b] *The Molecular Foundry, Lawrence Berkeley National Laboratory, 1 Cyclotron Road, Berkeley, CA 94720, USA. E-mail: bahelms@lbl.gov; Fax: +1 510 486 7413; Tel: +1 510 486 7729*
[c] *Computational Research Division, Lawrence Berkeley National Laboratory, 1 Cyclotron Road, Berkeley, CA 94720, USA*
[d] *Advanced Light Source, Lawrence Berkeley National Laboratory, 1 Cyclotron Road, Berkeley, CA 94720, USA*
[e] *Plasma Applications Group, Lawrence Berkeley National Laboratory, 1 Cyclotron Road, Berkeley, CA 94720, USA*
[f] *McKetta Department of Chemical Engineering, The University of Texas at Austin, Austin, TX 78712, USA*

† Electronic supplementary information (ESI) available: Materials & methods, Fig. S1–S16, Tables S1–S5. See DOI: 10.1039/c6cc10183f

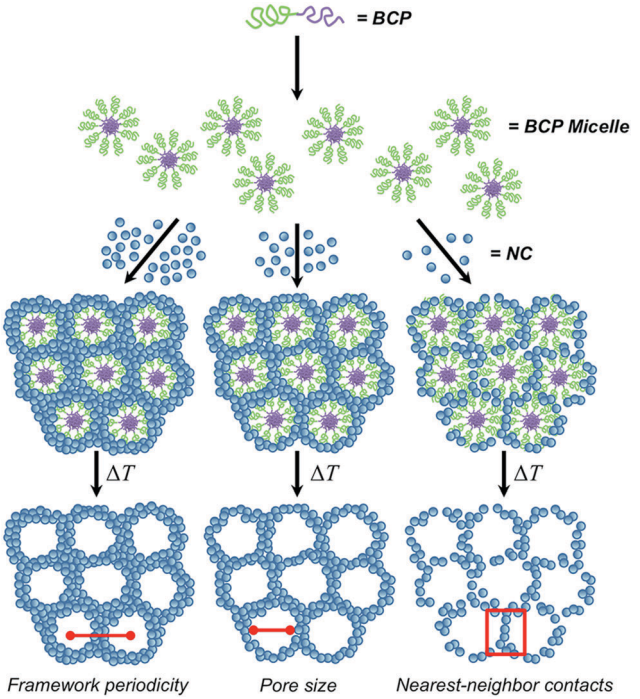

Scheme 1 Assembly trajectory for the preparation of mesoporous, colloidal nanocrystal frameworks and their analysis for framework periodicity, pore size, and nearest-neighbour contacts.

NCs and also reveal the mesopores (Scheme 1), with the ITO crystal structure remaining intact (Fig. S4, ESI†).

Regardless of the size of BCP micelle used as architecture-directing agent, we noted a trend in order to disorder in the CNF as the BCP loading in the initial mesostructured composite was increased. This was evidenced both in the top-down SEM and the associated GISAXS patterns (Fig. S5 (ESI†) for CNFs assembled with PS_{60k}-*b*-$PDMA_{20k}$ and Fig. S6 (ESI†) for CNFs assembled with PS_{20k}-*b*-$PDMA_{20k}$). To identify the order–disorder transition (ODT), top-down SEM images were segmented into binary images,[30] with pores indicated by black regions and NCs by white regions (Fig. 1 for CNFs assembled with PS_{60k}-*b*-$PDMA_{20k}$ and Fig. S7 (ESI†) for CNFs assembled with PS_{20k}-*b*-$PDMA_{20k}$). Next, a Voronoi tessellation algorithm was applied to determine the distribution of pixels from one pore centroid to the next, with borders drawn to indicate equal distances between adjacent pores; these borders segment the image into Voronoi cells. Finally, a frequency diagram was generated for the pore centroid-to-centroid orientation of surrounding Voronoi cells, with peaks indicating an ordered arrangement in the framework. For CNFs prepared from PS_{60k}-*b*-$PDMA_{20k}$ BCP micelles, the lowest BCP loadings (12–28% w/w) show Voronoi cells of regular size and shape; as BCP loading is increased (particularly for 44–60% w/w), the segmented cells become less defined and transform into disordered, irregular shapes. The same trend is seen in the distribution of pore centroid orientations within the Voronoi textures; peaks at −90°, 0°, and 90° significantly decrease in intensity at higher BCP loadings. Less intense peaks at −45° and +45° are indicative of short-range order—likely, mixed orientations

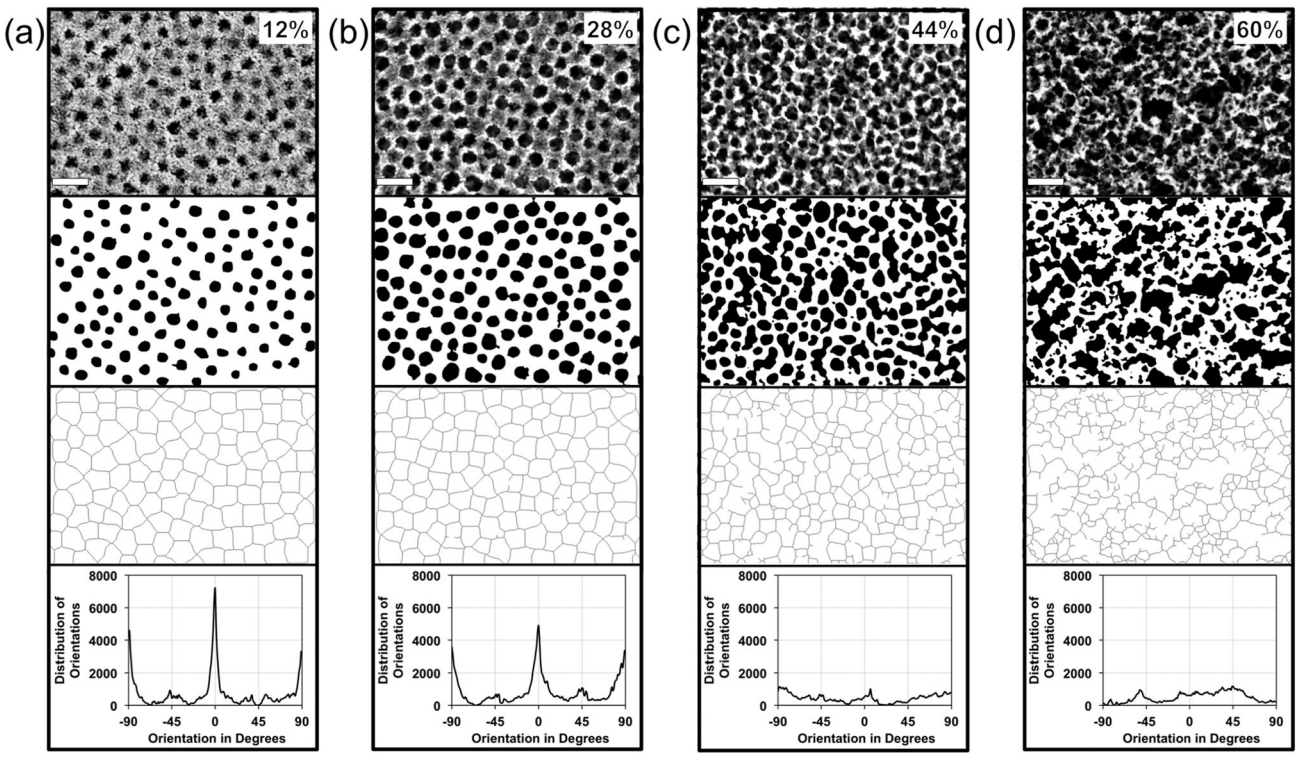

Fig. 1 Top-down SEM, binary segmentation, Voronoi diagram, and orientation analysis for CNFs or mesoporous NC films assembled with PS_{60k}-*b*-$PDMA_{20k}$ BCPs at a loading of either: (a) 12%; (b) 28%; (c) 44%; or (d) 60% w/w. Scale bar = 100 nm.

of one or more cubic lattices presented at the surface. For CNFs prepared from PS_{60k}-*b*-$PDMA_{20k}$ BCP micelles, the ODT occurs at a BCP loading of 36% w/w; for CNFs prepared from PS_{20k}-*b*-$PDMA_{20k}$ BCP micelles, the ODT occurs at a BCP loading of 28% w/w (see Fig. S8 & S9 for full range of data, ESI†).

Having identified the ODT for CNFs assembled with different BCP micelles, we were further interested in understanding how framework periodicity and other architectural metrics such as pore size and regularity varied with NC loading—*i.e.*, either above or below the ODT. To do so, line-traces were taken along the horizontal axis for each of the GISAXS scattering patterns (Fig. S10 & S11, ESI†) for CNFs assembled with either of the BCP architecture-directing agents. For CNFs assembled with PS_{60k}-*b*-$PDMA_{20k}$, we observed an invariant framework periodicity of ~51 nm (within experimental error) for BCP loadings of 12–36% w/w, which is consistent with the top-down SEM in Fig. 1. At these loadings, the frequency distribution of the Voronoi cells indicates this to be the ordered regime typical of CNFs. GISAXS gives further evidence of a higher degree of order in the CNF regime by the emergence of a secondary scattering peak (Fig. S10 & S11, ESI†).

Below the ODT, periodicity holds a more tenuous definition for these films, but nevertheless emerges as an observable in the GISAXS. Across these samples, the primary scattering peak broadened significantly and periodicity experienced a steep decline. This was concomitant with other framework irregularities visible by SEM, including disjunctions, where too few NCs are available to form the walls of the framework; mesopore coalescence was also observed in this regime. To distinguish these disordered films from ordered CNFs, we will refer to them simply as mesoporous NC films.

Further analysis of the segmented, binary SEM images gives insight into the pore structure (*i.e.*, pore area and circularity) above and below the ODT. Here, pore circularity is defined as $4\pi \times [\text{Area}/(\text{Perimeter})^2]$, with a value of 1.0 indicating a perfect circle. These results are most significant within the ordered CNF regime (*i.e.*, BCP loadings 12–36% w/w), which show the narrowest distribution in both pore area and circularity (Fig. 2). We estimated pore diameter from average pore area for these CNFs, and, while framework periodicity remained invariant, pore diameter steadily increased (*e.g.*, from 29 nm at 12% BCP loading w/w to 38 nm at 36% BCP loading). This indicates that NCs increasingly penetrate the PDMA corona of the micelle at higher NC loadings. Notably, then, framework periodicity is solely determined by the periodicity in packing of the BCP micelles; in this regard, they are indeed architecture-directing. Salient aspects of the architectural evolution between CNFs and mesoporous NC films—*i.e.*, above and below the ODT—were largely consistent for mesoporous films prepared using the smaller PS_{20k}-*b*-$PDMA_{20k}$ micelles as architecture-directing agent (Fig. S12, ESI†).

In that for disordered mesoporous NC films, there are too few NCs present to constitute a load-bearing segment (or wall) in the structure, it follows such films may also experience a film collapse during the thermal treatment used to rid the composite of the organic BCP micelles. Indeed, framework collapse at BCP loadings in excess of 52% w/w was evident after examining

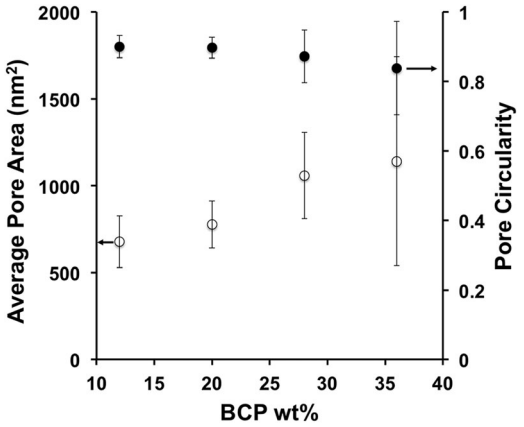

Fig. 2 Average pore area (open circles) and pore circularity (filled circles) *vs.* BCP loading for CNFs assembled with PS_{60k}-*b*-$PDMA_{20k}$. Pore diameters were: 29 nm at 12%, 31 nm at 20%, 36 nm at 28%, and 38 nm at 36% BCP loading w/w.

the films in cross-section using SEM (Fig. 3 & Fig. S15, ESI†). We also employed Rutherford Backscattering Spectroscopy (RBS) to determine f_{NC} for each film after thermal annealing; the expected trend would be for f_{NC} to increase with NC loading relative to BCP. However, this is not the case. At the highest BCP loading for both micelle sizes, the observed framework collapse leads to a higher f_{NC} than expected (Table S4, ESI†). In contrast, for ordered CNFs, cross-sectional analysis of the architecture by SEM confirmed the presence of well-formed, homogeneously-distributed mesopores throughout the films. Here, film thickness increased proportionally to the loading of NCs while the mass fraction of BCP was kept constant.

To better understand these outcomes, we quantified the average width of load-bearing segments in each film (Fig. S16 & S17, ESI†). For collapsed structures, *i.e.*, BCP loadings of >52% w/w, the average width of such segments (d_{seg}) was only 9.6 nm, which is less than the width of two NCs; the number of nearest-neighbours (and nearest-neighbour bonds) for each NC is therefore considerably smaller than for thicker load bearing segments. Specifically, we find film collapse for $d_{seg}/d_{NC} < 2$, stable mesoporous NC films for $2 < d_{seg}/d_{NC} < 3$, and stable CNFs $d_{seg}/d_{NC} > 3$. These relationships may vary by size-commensurability of NC and BCP components as well as their chemical composition and the annealing temperature.

The perspectives offered here indicate image analysis techniques, including matter segmentation and empty space estimation, are needed for more reliable and quantitative analysis of film architecture and differentiation among classes of mesoporous materials based on colloidal NCs. Our analysis showed that $d_{seg}/d_{NC} > 2$ is needed in the load-bearing segments to support the pore structure but that $d_{seg}/d_{NC} > 3$ is needed to assemble CNFs from 5.3 nm ITO NCs, offering more definitive insight into architecture than was afforded by reciprocal-space GISAXS analysis. We anticipate that this toolbox will apply to other multi-component, mesoporous materials, and thereby enable more deterministic explorations of meso-phase space than has been possible previously.

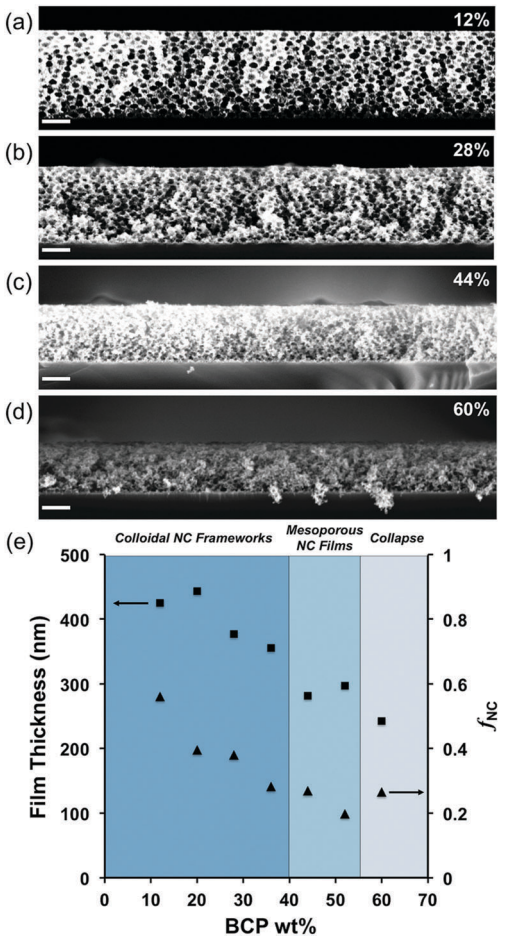

Fig. 3 Cross-sectional SEM for CNFs or mesoporous NC films assembled with PS_{60k}-*b*-$PDMA_{20k}$ BCPs at a loading of: (a) 12%; (b) 28%; (c) 44%; or (d) 60% w/w. Scale bar = 200 nm. (e) Film thickness (squares) & f_{NC} (triangles) *vs.* BCP loading.

GISAXS data were acquired at beamline 7.3.3 at the Advanced Light Source (ALS). RBS data were acquired at the Ion Beam Analysis Facility, operated by the Accelerator Technology and Applied Physics (ATAP) Division. Some image analysis algorithms were supported by the Center for Advanced Mathematics for Energy Related Applications (CAMERA). All other work was performed at The Molecular Foundry, which is supported by the Office of Science, Office of Basic Energy Sciences, of the U.S. Department of Energy under Contract No. DE-AC02-05CH11231. The ALS is supported by the Director, Office of Science, Office of Basic Energy Sciences, of the U.S. Department of Energy under the same contract. DJM is grateful for support from the Welch Foundation (F-1848).

Notes and references

1 S. C. Warren, L. C. Messina, L. S. Slaughter, M. Kamperman, Q. Zhou, S. M. Gruner, F. J. DiSalvo and U. Wiesner, *Science*, 2008, **320**, 1748.
2 T. Brezesinski, J. Wang, J. Polleux, B. Dunn and S. H. Tolbert, *J. Am. Chem. Soc.*, 2009, **131**, 1802.
3 R. Buonsanti, T. E. Pick, N. Krins, T. J. Richardson, B. A. Helms and D. J. Milliron, *Nano Lett.*, 2012, **12**, 3872.
4 I. E. Rauda, R. Buonsanti, L. C. Saldarriaga-Lopez, K. Benjauthrit, L. T. Schelhas, M. Stefik, V. Augustyn, J. Ko, B. Dunn, U. Wiesner, D. J. Milliron and S. H. Tolbert, *ACS Nano*, 2012, **6**, 6386.
5 Y. Liu, G. Stefanic, J. Rathousky, O. Hayden, T. Bein and D. Fattakhova-Rohlfing, *Chem. Sci.*, 2012, **3**, 2367.
6 J. B. Rivest, R. Buonsanti, T. E. Pick, L. Zhu, E. Lim, C. Clavero, E. Schaible, B. A. Helms and D. J. Milliron, *J. Am. Chem. Soc.*, 2013, **135**, 7446.
7 I. E. Rauda, L. C. Saldarriaga-Lopez, B. A. Helms, L. T. Schelhas, D. Membreno, D. J. Milliron and S. H. Tolbert, *Adv. Mater.*, 2013, **25**, 1315.
8 D. J. Milliron, R. Buonsanti, A. Llordes and B. A. Helms, *Acc. Chem. Res.*, 2014, **47**, 236.
9 B. A. Helms, T. E. Williams, R. Buonsanti and D. J. Milliron, *Adv. Mater.*, 2015, **27**, 5820.
10 A. W. Wills, D. J. Michalak, P. Ercius, E. R. Rosenberg, T. Perciano, D. Ushizima, R. Runser and B. A. Helms, *Adv. Funct. Mater.*, 2015, **25**, 4120.
11 G. K. Ong, T. E. Williams, A. Singh, E. Schaible, B. A. Helms and D. J. Milliron, *Nano Lett.*, 2015, **15**, 8240.
12 H. N. Lokupitiya, A. Jones, B. Reid, S. Guldin and M. Stefik, *Chem. Mater.*, 2016, **28**, 1653.
13 T. E. Williams, C. M. Chang, E. L. Rosen, G. Garcia, E. L. Runnerstrom, B. L. Williams, B. Koo, R. Buonsanti, D. J. Milliron and B. A. Helms, *J. Mater. Chem. C*, 2014, **2**, 3328.
14 J. Kim, G. K. Ong, Y. Wang, G. LeBlanc, T. E. Williams, T. M. Mattox, B. A. Helms and D. J. Milliron, *Nano Lett.*, 2015, **15**, 8240.
15 I. E. Rauda, V. Augustyn, L. C. Saldarriaga-Lopez, X. Chen, L. T. Schelhas, G. W. Rubloff, B. Dunn and S. H. Tolbert, *Adv. Funct. Mater.*, 2014, **24**, 6717.
16 J. B. Cook, H.-S. Kim, Y. Yan, J. S. Ko, S. Robbennolt, B. Dunn and S. H. Tolbert, *Adv. Energy Mater.*, 2016, **6**, 1501937.
17 B. K. Lesel, J. S. Ko, B. Dunn and S. H. Tolbert, *ACS Nano*, 2016, **10**, 7572.
18 I. Vamvasakis, K. S. Subrahmanyam, M. G. Kanatzidis and G. S. Armatas, *ACS Nano*, 2015, **9**, 4419.
19 I. T. Papadas, I. Vamvasakis, I. Tamiolakis and G. S. Armatas, *Chem. Mater.*, 2016, **28**, 2886.
20 K. Peters, H. N. Lokupitiya, D. Sarauli, M. Labs, M. Pribil, J. Rathouský, A. Kuhn, D. Leister, M. Stefik and D. Fattakhova-Rohlfing, *Adv. Funct. Mater.*, 2016, **26**, 6682.
21 J. Ba, J. Polleux, M. Antonietti and M. Niederberger, *Adv. Mater.*, 2005, **17**, 2509.
22 M. Zukalova, A. Zukal, L. Kavan, M. K. Nazeeruddin, P. Liska and M. Grätzel, *Nano Lett.*, 2005, **5**, 1789.
23 I. E. Rauda, V. Augustyn, B. Dunn and S. H. Tolbert, *Acc. Chem. Res.*, 2013, **46**, 1113.
24 N. Guijarro, M. S. Prevot, X. A. Jeanbourquin, X. Yu and K. Sivula, *Chem. Mater.*, 2015, **27**, 6337.
25 D. M. Lyons, K. M. Ryan and M. A. Morris, *J. Mater. Chem.*, 2002, **12**, 1207.
26 S. Wang, P. Tangvijitsakul, Z. Qiang, S. M. Bhaway, K. Lin, K. A. Cavicchi, M. D. Soucek and B. D. Vogt, *Langmuir*, 2016, **32**, 4077.
27 A. Dong, X. Ye, J. Chen, Y. Kang, T. Gordon, J. M. Kikkawa and C. B. Murray, *J. Am. Chem. Soc.*, 2011, **133**, 998.
28 E. L. Rosen, R. Buonsanti, A. Llordes, A. M. Sawvel, D. J. Milliron and B. A. Helms, *Angew. Chem., Int. Ed.*, 2012, **51**, 684.
29 S. E. Doris, J. J. Lynch, C. Li, A. W. Wills, J. J. Urban and B. A. Helms, *J. Am. Chem. Soc.*, 2014, **136**, 15702.
30 N. A. Hotaling, K. Bharti, H. Kriel and C. G. Simon Jr, *Biomaterials*, 2015, **61**, 327.

